Chinese Chemical Letters 33 (2022) 963–967

Contents lists available at ScienceDirect

Chinese Chemical Letters

journal homepage: www.elsevier.com/locate/cclet

A topotactic tailored synthesis of waxberry-like mixed-phase TiO_2 hollow spheres for dye-sensitized solar cells

Yang-Hong Wu[a], Kai-Yan Yuan[a], Yan-E He[a], Heng Wu[a], Li-Jiao Ma[a], Gang Wang[a], Xiao-Dong Qiao[a], Bing-Xin Lei[a,*], Zhen-Fan Sun[a], Zhao-Qing Liu[b,*]

[a] School of Chemistry and Chemical Engineering, Key Laboratory of Electrochemical Energy Storage and Energy Conversion of Hainan Province, Key Laboratory of Electrochemical Energy Storage and Light Energy Conversion Materials of Haikou City, Hainan Normal University, Haikou 571158, China
[b] School of Chemistry and Chemical Engineering/Institute of Clean Energy and Materials/Guangzhou Key Laboratory for Clean Energy and Materials/Huangpu Hydrogen Innovation Center, Guangzhou University, Guangzhou 510006, China

ARTICLE INFO

Article history:
Received 5 April 2021
Revised 25 June 2021
Accepted 9 July 2021
Available online 16 July 2021

Keywords:
Titanium dioxide
Phase composition
Topotactic methodology
Hollow sphere
Dye-sensitized solar cell

ABSTRACT

The waxberry-like mixed-phase TiO_2 hollow microstructures (WMTHMs) are controllably prepared *via* a topotactic synthetic method, involving the synthesis of monodispersed $CaTiO_3$ precursors by a solvothermal method and subsequently transforming them into TiO_2 through a Na_2EDTA-assisted ion-exchange process. The ratio of anatase-rutile is adjustable, and the two phases are connected well with each other. WMTHMs are composed of radially aligned nanorods, speeding up the electron transport. The optimum WMTHMs sample shows a specific surface area of 68.05 m^2/g and exhibits an excellent light scattering capacity. The cell based on WMTHMs light scattering layer obtained an optimal efficiency of 9.12%. The improvement of cell efficiency is mainly attributed to the high specific surface area, the efficient light scattering, the appropriate ratio of anatase-rutile, the staggered bandgap structure, and the convenient one-dimensional electron transport channel.

Since the pioneer work of O'Regan and Grätzel in 1991, the dye-sensitized solar cell (DSSC) has been a competitive photovoltaic device due to its advantages of low cost, easy of manufacture and remarkable energy conversion efficiency (η) [1,2]. To boost the total performance of DSSCs, many researchers have optimized components, such as photoanodes [3], electrolytes [4,5], sensitizers [6,7], and counter electrodes [8,9]. As one of the core components, the photoanode undertakes dye loading and charge transport. Among these studied photoanode materials, TiO_2 nanoparticle photoanode has attracted widespread attention due to its eco-friendliness, high chemical stability, and high specific surface area [10]. However, this kind of photoanode film reveals lower light scattering ability due to its smaller particle size [11]. Furthermore, TiO_2 nanoparticle photoanode has disordered electron transport channels, thereby affecting the charge transfer and collection efficiency.

As is well known, TiO_2 hollow structures are more effective to improve light scattering ability and facilitate the electrolyte diffusion than solid ones, which result in a better DSSCs performance [12,13]. The tailoring of TiO_2 hollow structures is a crucial means to improve the efficiency of DSSCs. Up to present, TiO_2 hollow structures with tailored textural properties are prepared through a variety of methods [14]. The most adopted method for the tailoring synthesis of hollow structure is a template method, including hard templates (mono-dispersed silica [15,16] or polystyrene beads [17,18]) or soft templates (surfactant micelles/vesicles [19], emulsion droplets [20] or gas bubbles [21]). For $CaTiO_3$ templates, Ca^{2+} is easily exchanged from the perovskite Ti-O frameworks in an acidic medium [22]. $CaTiO_3$ is chosen to act as self-template for the formation of TiO_2 via a topotactic synthetic method, which is in favor of tailoring desirable morphology. Due to the well-matched lattice spacings between $CaTiO_3$ and TiO_2, TiO_2 can perfectly inherit the $CaTiO_3$ morphology, guaranteeing a strong mechanical stability of TiO_2 structure.

In addition, the anatase/rutile-mixed phase TiO_2 is an effective photoanode material. The tailoring of the ratio of anatase-rutile is very important to enhance the performance of DSSCs. For the preparation of anatase/rutile-mixed phase TiO_2, two kinds of preparation methods are popular. One of the preparation methods is a mechanical mixing method, which cannot guarantee that the two phases are in close contact and the electron-hole pair separates effectively. The annealing treatment is another preparation method, which easily leads to particle aggregation. Therefore, for

* Corresponding authors.
E-mail addresses: leibx@hainnu.edu.cn (B.-X. Lei), lzqgzu@gzhu.edu.cn (Z.-Q. Liu).

https://doi.org/10.1016/j.cclet.2021.07.032
1001-8417/

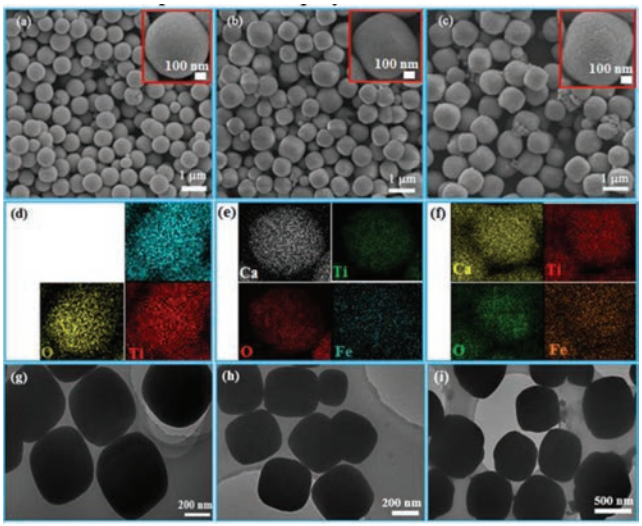

Fig. 1. FESEM, EDS mapping and TEM images of $CaTiO_3$-Fe_n precursors: (a, d and g) $CaTiO_3$-Fe_0, (b, e and h) $CaTiO_3$-Fe_1 and (c, f and i) $CaTiO_3$-Fe_2. The inset is high-resolution FESEM images.

the tailoring of TiO_2 hollow structures, it is crucial to adopt a suitable preparation method concentrating various functions.

In this work, the waxberry-like mixed-phase TiO_2 hollow microstructures (WMTHMs) were fabricated via a topotactic synthetic method. WMTHMs are composed of radial TiO_2 nanorods. The ratio of rutile-anatase can be changed by adding $FeCl_3$. The optimized DSSCs of the assembled double-layer P25 + WMTHMs photoanode obtained an excellent η of 9.12%, which was superior to the DSSC of the pure P25 photoanode (8.12%).

Fig. 1 shows the FESEM, EDS mapping and TEM images of the as-prepared $CaTiO_3$-Fe_n precursors. As shown in Figs. 1a-c, the as-prepared $CaTiO_3$-Fe_n precursors are nearly spherical structure in shape and their surfaces are rather smooth. The individual spheres are mutually separated without aggregation. As the amount of $FeCl_3$ increases, the shape of the $CaTiO_3$-Fe_n spheres is not changed, but the diameter of $CaTiO_3$-Fe_n varies from 120 to 160 and 270 nm. The EDS mapping of $CaTiO_3$-Fe_0 (Fig. 1d) clearly reveals that the three elements (Ca, Ti, and O) are evenly distributed throughout the sample. The EDS mappings of $CaTiO_3$-Fe_1 (Fig. 1e) and $CaTiO_3$-Fe_2 (Fig. 1f) indicate that the four elements (Ca, Ti, O and Fe) are distributed over the entire samples. TEM results (Figs. 1g-i) confirm that all $CaTiO_3$-Fe_n precursors display a solid structure.

XRD patterns of the as-prepared $CaTiO_3$-Fe_n precursors are shown in Fig. S1a (Supporting information). XRD patterns of $CaTiO_3$-Fe_1 and $CaTiO_3$-Fe_2 are similar to that of $CaTiO_3$-Fe_0. The diffraction peaks (2θ = 23.2°, 33.1°, 38. 9°, 40.7°, 47.5°, 53.3°, 59.3°, 69.5° and 79.1°) correspond to the (101), (121), (211), (220), (202), (301), (042), (242) and (323) planes of perovskite-type $CaTiO_3$ (JCPDS No. 42-0423). Nevertheless, the Fe-containing species are not detected by XRD, which may be attributed to the low content in $CaTiO_3$-Fe_1 and $CaTiO_3$-Fe_2. Fig. S1b (Supporting information) shows the enlarged XRD curves of $CaTiO_3$-Fe_n in the range of 31-35°. With increasing Fe content, the (121) diffraction peak gradually shifts to a larger angle, verifying the distortion of $CaTiO_3$ crystal lattice by Fe dopant. It is well known that Ti^{4+} (0.75 Å) and Fe^{3+} (0.79 Å) have similar ionic radius, which may lead to the exchange of Ti^{4+} and Fe^{3+} in $CaTiO_3$ for the formation of new species [23]. Fe may also exist in Fe_2O_3 from the reaction of $FeCl_3$ during a solvothermal process. For $CaTiO_3$-Fe_1 and $CaTiO_3$-Fe_2, Fe may exist in Fe_2O_3 or the formation of new species.

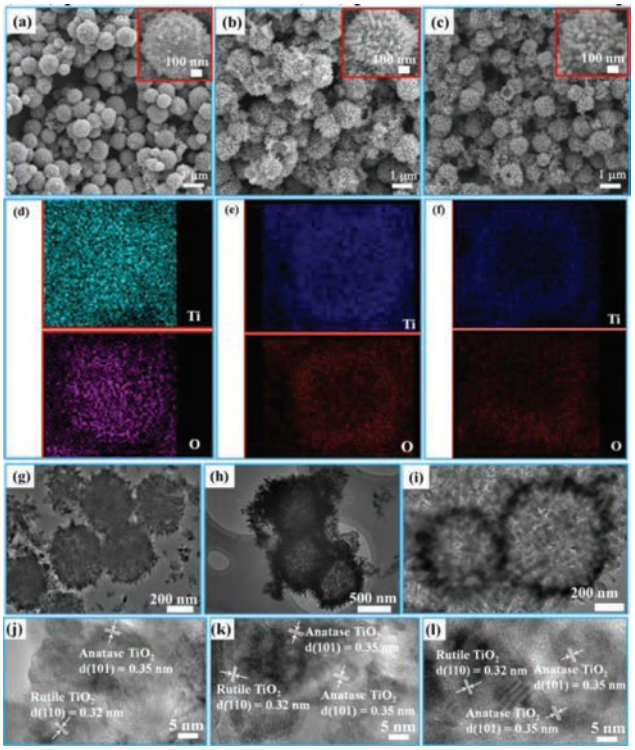

Fig. 2. FESEM, EDS mapping, TEM and HRTEM images of WMTHMs: (a, d, g and j) WMTHMs-0, (b, e, h and k) WMTHMs-1 and (c, f, i and l) WMTHMs-2.

The surface chemical states of $CaTiO_3$-Fe_1 and $CaTiO_3$-Fe_2 are characterized by XPS (Fig. S2 in Supporting information). Fig. S2a shows the survey spectra of $CaTiO_3$-Fe_1. For the XPS spectra of Ca 2p (Fig. S2b), the major peaks at 349.8 eV and 346.3 eV correspond to the binding energies of Ca $2p_{1/2}$ and Ca $2p_{3/2}$, respectively. For the XPS spectra of Ti 2p (Fig. S2c), the two major peaks, centered at around 458.1 eV and 463.8 eV, are ascribed to Ti $2p_{3/2}$ and Ti $2p_{1/2}$ of the Ti^{4+} states, respectively. For the XPS spectra of O 1s (Fig. S2d), the major peak centered at 529.5 eV can be attributed to the Ti-O band, which corresponds to the O^{2-} state in the lattice of $CaTiO_3$-Fe_1. For the XPS spectra of Fe 2p (Fig. S2e), the Fe $2p_{3/2}$ peak at 710.2 eV corresponds to Fe^{3+} state [24]. In XPS spectra, there is no significant difference between $CaTiO_3$-Fe_1 (Figs. S2a-e) and $CaTiO_3$-Fe_2 (Figs. S2f-j). The results demonstrate that the Fe-containing species exists in $CaTiO_3$-Fe_1 and $CaTiO_3$-Fe_2.

Fig. 2 shows the FESEM, EDS mapping and TEM images of the as-prepared WMTHMs-n samples. As shown in Fig. 2a, the WMTHMs-0 is composed of a large quantity of uniform, rough spheres with a diameter of around 0.95-1.10 μm. The high-resolution FESEM (inset of Fig. 2a) displays a waxberry-like TiO_2 hollow sphere. Observingly, WMTHMs-0 consists of tiny short rods with dense state. With increasing the Fe content in the precursor, the diameter of WMTHMs-1 (Fig. 2b) increases to 1-1.30 μm, and the external structure of spheres has changed. The high-resolution FESEM (inset of Fig. 2b) displays the WMTHMs-1 is composed of nanorods with a diameter of about 70-80 nm, and the growth direction of these nanorods is nearly radially on the external surface of sphere. Moreover, the hollow interior is clearly observed from some broken spheres, which is favorable for enhancing the light scattering ability. With further increasing the Fe content in the precursor, as shown in Fig. 2c, WMTHMs-2 shows the same external structure as WMTHMs-1. WMTHMs-2 with a diameter of 1-1.20 μm is also composed of nanorods with a diameter of about 45-55 nm. The EDS mapping images (Figs. 2d-f) indicate that Ti and O elements are distributed homogeneously in three kinds of WMTHMs.

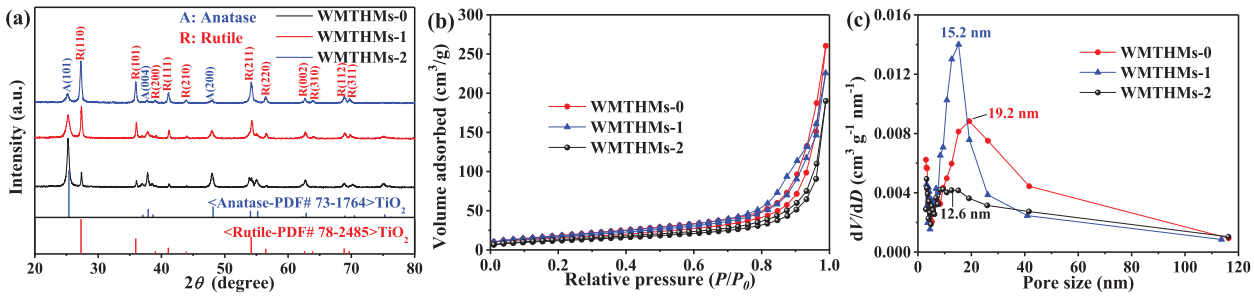

Fig. 3. (a) XRD patterns, (b) N_2 adsorption-desorption isotherms and (c) pore size distribution curves of WMTHMs-0, WMTHMs-1 and WMTHMs-2.

The as-prepared WMTHMs-n samples are further characterized by TEM. In Fig. 2g, WMTHMs-0 consists of tiny nanorods and displays a hollow structure. In the case of little amount of $FeCl_3$ added, WMTHMs-1 (Fig. 2h) and WMTHMs-2 (Fig. 2i) samples are composed of radially arranged nanorods and display a hollow structure. Ca^{2+} ions are exchanged with H^+ ions in the presence of Na_2EDTA. The out-diffusion rate of Ca^{2+} ions is much faster than the in-diffusion rate of H^+ ions, which results in the formation of hollow structure [25]. TiO_2 evolves from $CaTiO_3$ by a dissolution-recrystallization process. Meanwhile, Fe-containing species are removed with the assistance of Na_2EDTA. For WMTHMs-n, Figs. 2j-l demonstrate that the lattice spacings of 0.32 nm and 0.35 nm correspond to the (110) plane of rutile and the (101) plane of anatase TiO_2, respectively.

The composition of WMTHMs-n is confirmed by XRD (Fig. 3a). The diffraction peaks at $2\theta = 37.9°$ and 48.2° are indexed to the (004), (200) crystal planes of anatase TiO_2 (JCPDS No. 73-1764). Other peaks at $2\theta = 36.1°$, 41.2°, 54.3°, 56.6°, 62.8°, 69.8° and 72.4°, are indexed to the (101), (111), (211), (220), (002), (112) and (311) crystal planes of rutile TiO_2 (JCPDS No. 78-2485). For all the as-prepared WMTHMs-n, the coexisting anatase and rutile phases are in agreement with TEM. As expected, the anatase/rutile mixed TiO_2 has excellent charge separation efficiency [26,27]. The ratio of rutile-anatase can be calculated by the following Eqs. 1 and 2 [28]:

$$W_r = \frac{A_r}{A_r + 0.884A_a} \quad (1)$$

$$W_a = 1 - W_r \quad (2)$$

here, W_r, W_a, A_a and A_r represent the rutile content, the anatase content, the integrated intensity of anatase (101) peak, and the integrated intensity of rutile (110) peak, respectively. The ratio of anatase-rutile is listed in Table S1 (Supporting information). The result indicates that the ratio of anatase-rutile is affected by the Fe content of the precursor. With the increase of Fe content in the precursor, the rutile content increases. That is to say, the ratio of anatase-rutile in WMTHMs-n can be successfully controlled by simply adjusting the amount of $FeCl_3$. XRD patterns of the WMTHMs-1 and WMTHMs-2 show no traces of other phases like Fe_2O_3 or Fe_xTiO_y. It is believed that the ion-exchange reaction may occur between Fe-containing species and H^+ with the assistance of Na_2EDTA.

As we know, both Ti^{4+} ion (0.75 Å) and Fe^{3+} ion (0.79 Å) have similar ion radius, which indicates that Fe^{3+} ions may enter $CaTiO_3$ lattice to replace Ti^{4+} sites [23]. Based on simple charge compensation grounds, the formation of oxygen vacancies would generate due to the substitutional incorporation of Fe^{3+}, which can offer space for the atomic arrangement [29]. Besides, the oxygen vacancies increase with increasing Fe content, so the mass fraction of rutile phase increases with increasing Fe content [29]. During transformation $CaTiO_3$-Fe into TiO_2 through a Na_2EDTA-assisted ion-exchange process, Fe content can affect the ratio of anatase-rutile in WMTHMs.

The co-existence of anatase and rutile phases in the WMTHMs-1 and WMTHMs-2 is further characterized by Raman spectroscopy (Fig. S3 in Supporting information). The peaks appeared at 147 cm^{-1} (E_g), 397 cm^{-1} (B_{1g}), 512 cm^{-1} (A_{1g}) and 639 cm^{-1} (E_g) are well matched with the anatase TiO_2 modes. The three peaks of rutile centered at 239, 445 and 614 cm^{-1} are attributed to multi-proton process, E_g and A_{1g} of the rutile modes [30]. It clearly indicates that both WMTHMs-1 and WMTHMs-2 are made of anatase and rutile phases, without other phases like Fe_2O_3 or Fe_xTiO_y, which is also in agreement with XRD results.

The surface characterization of WMTHMs-1 and WMTHMs-2 are performed by XPS. As shown in Fig. S4a (Supporting information), the XPS survey spectra of WMTHMs-1 show the existence of Ti and O elements and the absence of Fe^{3+}. In Fig. S4b (Supporting information), the two peaks, presented at around 463.8 eV and 458.1 eV, are attributed to Ti $2p_{1/2}$ and Ti $2p_{3/2}$ of the dominant Ti^{4+} state, respectively [31]. In Fig. S4c (Supporting information), the peak at 529.4 eV is ascribed to the lattice oxygen in TiO_2, indicating the presence of an oxygen environment. In XPS spectra, there is no significant difference between WMTHMs-2 (Figs. S4d-f in Supporting information) and WMTHMs-1 (Figs. S4a-c in Supporting information).

The BET specific surface area and pore size distribution of WMTHMs-n samples are investigated by N_2 adsorption-desorption measurement. In Fig. 3b, all N_2 adsorption-desorption isotherms show typical IV-type isotherms with an H2 hysteresis loop according to IUPAC classification, which are characteristic of mesoporous materials [32,33]. The WMTHMs-0 and WMTHMs-1 samples exhibit ideal specific surface area of 64.76 m^2/g and 68.05 m^2/g, respectively, which are higher than WMTHMs-2 (43.41 m^2/g) and the commercial P25 (~50 m^2/g). Therefore, the WMTHMs-0 and WMTHMs-1 samples can facilitate the dye adsorption of DSSCs. Fig. 3c reveals the corresponding pore size distribution of WMTHMs-n samples. With the increase of Fe content in the precursor, the pore diameter has a decrease. The pore size of the as-prepared WMTHMs-0, WMTHMs-1 and WMTHMs-2 are 19.2, 15.2, and 12.6 nm, respectively. The relatively wide pore size distributions are beneficial to electrolyte diffusion. This result indicates the Fe content of the precursor exerts a great effect on the textural structure.

The *J-V* curves are displayed in Fig. 4a and their corresponding photovoltaic characteristics (J_{sc}: short-circuit current density, V_{oc}: open-circuit voltage, *FF*: fill factor, and η) are summarized in Table 1. From Table 1, the four cells have a similar *FF*, while both J_{sc} and η exhibit an increase and then decrease with the increasing Fe content in the precursor. The cells based on WMTHMs-0 and WMTHMs-1 scattering layer photoanodes have achieved higher η (8.38% and 9.12%) than that of the Cell-P25 without scattering layer (8.12%). However, introducing an additional scattering layer of WMTHMs-2, the η of Cell-P25 + WMTHMs-2 decrease to 7.96%.

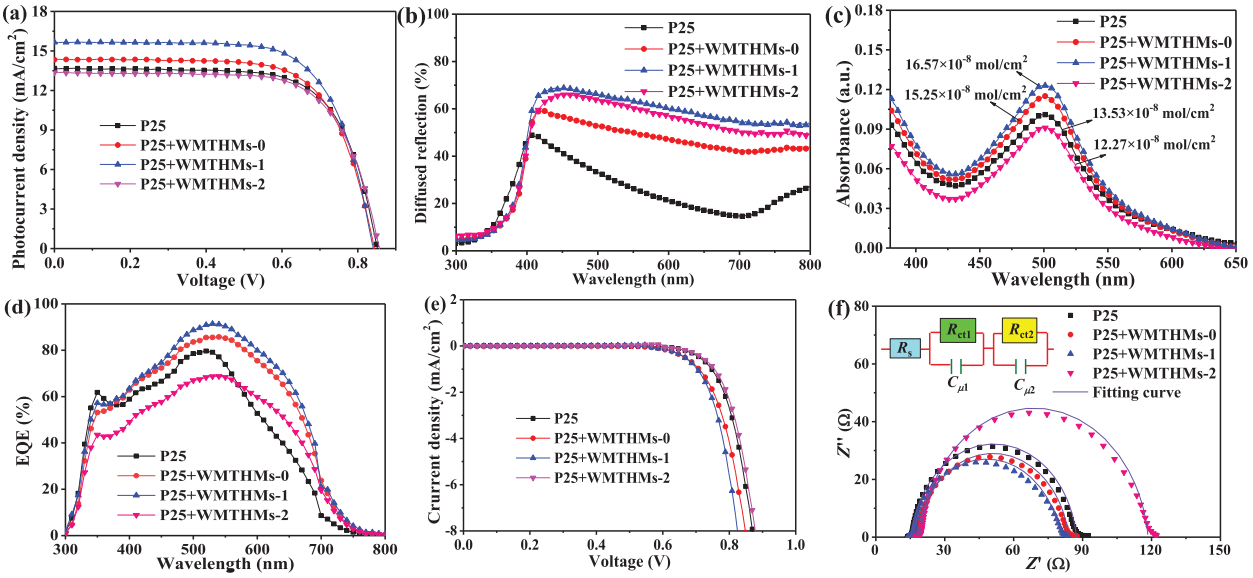

Fig. 4. (a) *J-V* curves, (b) diffuse reflectance spectra, (c) UV-vis absorption spectra, (d) EQE spectra, (e) dark *J-V* and (f) EIS curves of DSSCs based on different photoanode films.

Table 1
Detailed photovoltaic parameters of DSSCs based on different photoanode films.

Cell	V_{oc} (V)	J_{sc} (mA/cm^2)	*FF* (%)	η (%)	R_s (Ω)	R_{ct1} (Ω)	R_{ct2} (Ω)	$C_{\mu 2}$ (μF)	τ_e (ms)
P25	0.855	13.66	69.78	8.12	14.14	0.94	69.19	941.37	65.13
P25 + WMTHMs-0	0.843	14.36	69.16	8.38	16.57	0.85	63.12	922.48	58.23
P25 + WMTHMs-1	0.840	15.65	69.34	9.12	14.12	0.92	61.36	898.95	55.16
P25 + WMTHMs-2	0.857	13.35	69.52	7.96	17.52	0.96	95.38	937.78	89.45

The η initially increases from 8.38% to 9.12% with the increasing Fe content in the precursor, which is attributed to the synergistic effects of the appropriate ratio of anatase-rutile, the convenient one-dimensional electron transport channel, the superior light scattering ability and the higher dye loading amounts. The mixed-phase TiO_2 can form a synergistic effect between anatase and rutile crystals. The photo-generated electrons coming from N719 inject into the rutile phase TiO_2 and then migrate to the anatase phase TiO_2. Such staggered bandgap can suppress charge recombination, thereby improving the efficiency of DSSCs. However, when the Fe content of the precursor is further increased, the η decreases from 9.12% to 7.96%, which may be due to the unsuited ratio of anatase-rutile, the inferior light scattering capacity and the lower dye loading amounts. Compared with $CaTiO_3$-Fe_n light scattering layer, the DSSCs based on the WMTHMs-n show higher efficiency, as shown in Fig. S5 and Table S2 (Supporting information).

It is well known that the J_{sc} is closely related to the light scattering capacity and the amounts of dye loading. To study the effect of light scattering capacity on the J_{sc}, the diffuse reflection property of the as-prepared photoanode films without N719 dye loading is investigated. In Fig. 4b, the diffuse reflection property of P25 + WMTHMs-0, P25 + WMTHMs-1 and P25 + WMTHMs-2 films is obviously higher than that of the pure P25 film, which is expected to exhibit a better light scattering capability of the WMTHMs-n layer. For the WMTHMs-n, besides that the comparable sphere size to the wavelength of visible light plays an important role in enhancing light scattering, their hollow structure can confine the incident light within the photoanode by light refraction between the wall and the air-filled pore, as shown in Fig. S6 (Supporting information).

The amounts of N719 dye anchored on the four films are investigated using 0.1 mol/L NaOH solution. UV-vis absorption spectra of dye molecules are shown in Fig. 4c. The order of dye loading capability is: Cell-P25 + WMTHMs-1 (16.57×10^{-8} mol/cm^2) > Cell-P25 + WMTHMs-0 (15.25×10^{-8} mol/cm^2) > Cell-P25 (13.53×10^{-8} mol/cm^2) > Cell-P25 + WMTHMs-2 (12.27×10^{-8} mol/cm^2), which are closely related to their BET specific surface areas and ratio of anatase-rutile. Due to the higher light scattering capacity and bigger dye loading capability, Cell-P25 + WMTHMs-1 demonstrates an optimum J_{sc}.

The differences in J_{sc} of the four cells are further investigated by measuring EQE spectra. Fig. 4d shows the EQE spectra as a function of wavelength for the four cells. The high EQE values in the short wavelength range are mainly attributed to the higher dye loading capability, and the somewhat higher EQE values in the long wavelength range of 600-750 nm are ascribed to the more efficient light scattering of the WMTHMs-n layer. Considering that dye loading capability and the diffuse reflection, Cell-P25 + WMTHMs-1 possesses higher EQE values over a wide range than Cell-P25. However, Cell-P25 + WMTHMs-1 shows lower EQE values than Cell-P25 in the short wavelength range, whereas it is just the opposite in the long wavelength range.

The dark *J-V* characteristics reflects the recombination of injected electrons with I_3^-. In Fig. 4e, the dark current densities of the Cell-P25 + WMTHMs-n are 4.09, 5.51 and 2.35 mA/cm^2 at 0.80 V, respectively. On the contrary, the P25 + WMTHMs-2 electrode displays a low current density, indicating the low recombination loss. The relatively high dark current density of P25 + WMTHMs-1 electrode means a high interface recombination loss, which could be explained by the enlarged recombination. The high recombination loss leads to a decrease in V_{oc}, which is agreement with the V_{oc} value.

To further make out the electron transport and interface recombination process in the four cells, EIS of Cell-P25 + WMTHMs-n are measured (Fig. 4f). In Fig. 4f, the smaller semicircle is assigned to the charge transfer resistance (R_{ct1}) at the electrolyte/Pt

counter electrode, while the larger semicircle is assigned to the charge recombination resistance (R_{ct2}) at the TiO_2/dye/electrolyte interfaces. The C_μ represents the chemical capacitance. The data are analyzed using Z-view software with an equivalent circuit (inset of Fig. 4f). The EIS parameters are listed in Table 1. The R_s and R_{ct1} values are almost identical because of the similar substrate, counter electrode, and I^-/I_3^- electrolyte. From Table 1, the R_{ct2} of the four cells are distinguishing, and the order of R_{ct2} value is: Cell-P25 + WMTHMs-2 (95.38 Ω) > Cell-P25 (69.19 Ω) > Cell-P25 + WMTHMs-0 (63.12 Ω) > Cell-P25 + WMTHMs-1 (61.36 Ω). Based on the fitted R_{ct2} and $C_{\mu 2}$, the electron lifetime ($\tau_e = R_{ct2} \times C_{\mu 2}$) values are calculated to be 58.23, 55.16, 89.45 and 65.13 ms for Cell-P25 + WMTHMs-0, Cell-P25 + WMTHMs-1, Cell-P25 + WMTHMs-2 and Cell-P25, respectively. Obviously, the Cell-P25 + WMTHMs-1 shows the shortest τ_e, manifesting that Cell-P25 + WMTHMs-1 has the quickest electron recombination process. This may be attributed to the large surface area of WMTHMs-1 introduced many defects. This leads to rapid recombination of electrons at the photoanode/dye/electrolyte interface, which in turn reflects a shortening τ_e for Cell-P25 + WMTHMs-1 [34]. The shorter τ_e for the Cell-P25 + WMTHMs-1 also further supports its lower V_{oc}. The undesired V_{oc} for P25 + WMTHMs-1 electrode can be compensated by the high J_{sc} due to the efficient light scattering and superior dye loading capability, making Cell-P25 + WMTHMs-1 endow a marked efficiency.

In this study, the anatase/rutile mixed TiO_2 hollow spheres were fabricated via a topotactic synthetic method using monodispersed $CaTiO_3$ precursor templates. The ratio of anatase-rutile was controlled through adding $FeCl_3$ content. WMTHMs-1 sample exhibited the best light scattering property and highest specific surface area. A double-layer photoanode consisting of WMTHMs-n used as light scattering layer and P25 as underlayer was designed. The DSSCs of the assembled double-layer P25 + WMTHMs-n photoanodes obtained a η of 8.38%, 9.12% and 7.96%, respectively. A maximum η of 9.12% was achieved by using the P25 + WMTHMs-1 bilayer photoanode, showing a marked improvement compared with the pure P25 photoanode (8.12%). The improvement of the efficiency was mainly attributed to the structure of WMTHMs-1, which can provide multiple scattering centers to enhance the light harvesting ability, the direct pathways for fast electron transfer, the appropriate ratio of anatase-rutile for quick charge separation, the staggered bandgap structure, and the high specific surface area for adsorbing dye.

Declaration of competing interest

The authors declare that they have no known competing financial interests or personal relationships that could have appeared to influence the work reported in this paper.

Acknowledgements

This work is financially supported by the National Natural Science Foundation of China (No. 21965013), the Natural Science Foundation of Hainan Province (No. 220RC590), and the Graduate Student Research and Innovation Program of Hainan Province (No. hsyx2019-17).

Supplementary materials

Supplementary material associated with this article can be found, in the online version, at doi:10.1016/j.cclet.2021.07.032.

References

[1] B. O'Regan, M. Grätzel, Nature 353 (1991) 737–740.
[2] U. Bach, D. Lupo, P. Comte, et al., Nature 395 (1998) 583–585.
[3] F. Bella, G. Griffini, M. Gerosa, S. Turri, R. Bongiovanni, J. Power Sources 283 (2015) 195–203.
[4] J.K. Kim, C.S. Lee, S.Y. Lee, H.H. Cho, J.H. Kim, J. Power Sources 336 (2016) 286–297.
[5] A. Yella, H.W. Lee, H.N. Tsao, et al., Science 334 (2011) 629–634.
[6] Y. Tang, X. Liu, Y. Wang, et al., Chin. Chem. Lett. 31 (2020) 1927–1930.
[7] Y.K. Eom, I.T. Choi, S.H. Kang, et al., Adv. Energy. Mater. 5 (2015) 1500300.
[8] J. Dong, J.H. Wu, J.B. Jia, et al., J. Power Sources 336 (2016) 83–90.
[9] J. Gao, Y. Yang, Z. Zhang, et al., Nano. Energy 26 (2016) 123–130.
[10] E.J.W. Crossland, N. Noel, V. Sivaram, et al., Nature 495 (2013) 215–219.
[11] Z.S. Wang, H. Kawauchi, T. Kashima, H. Arakawa, Coord. Chem. Rev. 248 (2004) 1381–1389.
[12] S. Hore, P. Nitz, C. Vetter, et al., Chem. Commun. 15 (2005) 2011–2013.
[13] Y.W. Zhang, J. Zhang, P.Q. Wang, et al., Mater. Chem. Phys. 123 (2010) 595–600.
[14] F. Zhu, D.P. Wu, Q. Li, et al., RSC Adv. 2 (2012) 11629–11637.
[15] M.J. Zhou, Y.C. Liu, J. Chen, X.L. Yang, J. Mater. Chem. A 3 (2015) 1068–1076.
[16] T. Leshuk, S. Linley, G. Baxter, F. Gu, ACS Appl. Mater. Interfaces 4 (2012) 6062–6070.
[17] F.Q. Liu, J. Su, W. Wang, et al., J. Mater. Chem. A 3 (2015) 3136–3143.
[18] P.L. Ji, X.Z. Kong, J.G. Wang, X.L. Zhu, Chin. Chem. Lett. 23 (2012) 1399–1402.
[19] J. Rao, A. Yu, C.L. Shao, X.F. Zhou, ACS Appl. Mater. Interfaces 4 (2012) 5346–5352.
[20] W.W. Cai, H. Yang, X.Z. Guo, Chin. Chem. Lett. 25 (2014) 441–446.
[21] S. Cheng, D. Yan, J.T. Chen, et al., J. Phys. Chem. C 113 (2009) 13630–13635.
[22] Q.L. Wu, X.F. Yang, W.Z. Zhou, et al., Adv. Mater. Interfaces 2 (2015) 1500210.
[23] C. Han, H. Yang, X.X. Xue, Trans. Nonferrous Met. Soc. China 24 (2014) 3215–3220.
[24] L. He, Y.N. Dong, Y.E. Zheng, et al., J. Hazard. Mater. 361 (2018) 85–94.
[25] X. Gao, G. Li, Y. Xu, et al., Angew. Chem., Int. Ed. 54 (2015) 14331–14335.
[26] Y.K. Hwang, S.S. Park, J.H. Lim, Y.S. Won, S. Huh, J. Nanosci. Nanotechnol. 13 (2013) 2255–2261.
[27] G.H. Li, C.P. Richter, R.L. Milot, et al., Dalton Trans. (2009) 10078–10085.
[28] H.Z. Zhang, J.F. Banfield, J. Phys. Chem. B 104 (2000) 3481–3487.
[29] Q. Gao, X.M. Wu, Y.M. Fan, Dyes Pigments 95 (2012) 96–101.
[30] C.C. Jia, X. Zhang, P. Yang, Appl. Surf. Sci. 430 (2018) 457–465.
[31] H. Khan, I.K. Swati, Ind. Eng. Chem. Res. 55 (2016) 6619–6633.
[32] Y. Ding, L.E. Mo, L. Tao, et al., Nano 9 (2014) 1440007.
[33] T. Zhao, Y. Ren, G. Jia, et al., Chin. Chem. Lett. 30 (2019) 2032–2038.
[34] G.J. Ke, H.Y. Chen, C.Y. Su, D.B. Kuang, J. Mater. Chem. A 1 (2013) 13274–13282.